Polarization state conversion achieved by chiral mechanical metamaterial

Hicham Mangach, Younes Achaoui, Muamer Kadic, Abdenbi Bouzid, Sébastien Guenneau, Shuwen Zeng

PAPER • OPEN ACCESS

Polarization state conversion achieved by chiral mechanical metamaterial

IOP Publishing New J. Phys. 26 (2024) 023053 https://doi.org/10.1088/1367-2630/ad2745

New Journal of Physics
The open access journal at the forefront of physics

Deutsche Physikalische Gesellschaft DPG
IOP Institute of Physics

Published in partnership with: Deutsche Physikalische Gesellschaft and the Institute of Physics

OPEN ACCESS

RECEIVED
19 June 2023

REVISED
26 January 2024

ACCEPTED FOR PUBLICATION
7 February 2024

PUBLISHED
27 February 2024

PAPER

Polarization state conversion achieved by chiral mechanical metamaterial

Hicham Mangach[1,2], Younes Achaoui[2], Muamer Kadic[3], Abdenbi Bouzid[2], Sébastien Guenneau[4,5] and Shuwen Zeng[1,*]

[1] Light, Nanomaterials Nanotechnologies (L2n) Laboratory, CNRS UMR 7076, Université de Technologie de Troyes, Troyes 10000, France
[2] Laboratory of Optics, Information Processing, Mechanics, Energetics and Electronics, Department of Physics, Moulay Ismail University, B.P. 11201, Zitoune, 50000 Meknes, Morocco
[3] Université de Franche-Comté, Institut FEMTO-ST, CNRS, Besançon 25000, France
[4] UMI 2004 Abraham de Moivre-CNRS, Imperial College London, SW7 2AZ London, United Kingdom
[5] The Blackett Laboratory, Physics Department, Imperial College London, SW7 2AZ London, United Kingdom
* Author to whom any correspondence should be addressed.

E-mail: shuwen.zeng@cnrs.fr

Keywords: chiral metamaterial, micro-rotation, polarization control, monatomic mass-in-mass unit cell

Abstract

Recently, metamaterials have driven advancements in wave propagation and polarization control. Chiral elastic metamaterials, in particular, have attracted considerable attention due to their distinctive properties, such as acoustical activity and auxeticity. Such characteristics arise from the additional degrees of freedom for tuning the embedded micro- and macro-rotations. In this study, we demonstrate an unusual energy exchange between longitudinal and in-plane shear waves in a 3D chiral mechanical metamaterial. The structural design is capable of inducing up to a 90° rotation in the plane of polarization. Additionally, this capacity for conversion is achieved by employing both an arrangement of chiral cells and a single meta-atom. This peculiar behavior enables a seamless switch between the three polarization states existing within a solid material, namely, the longitudinal state, the shear horizontal state, and the shear vertical state. Furthermore, a 2D discrete mono-atomic mass-spring model featuring inclined connectors is used to characterize the distinctive energy exchange between modes. This characterization is based on the retrieval of the pertinent elastic coefficients. The engineered chiral metamaterial polarization converter stands as a promising device for momentum conservation conversions and applications in elasto-dynamic polarimetry.

1. Introduction

Recently, the subject of artificially engineered materials has undoubtedly gained prominence and elicited widespread interest [1]. Symmetry breaking in chiral structures is an important mechanism for numerous physical phenomena [2–5]. Notably, the circular dichroism [6, 7] is also obtained by chirality. Additionally, circular birefringence based on chiral structures enables the rotation of the plane of light oscillation, and the emergence of quasi-dark states in the continuum [8–10]. In this context, Yonghao *et al* demonstrate a strong optical activity in dual-layered twisted arcs metamaterial with a polarization rotatory of about 305° [11].

Significant advancements have been made in the field of chiral mechanical metamaterials, demonstrating progress at both the micro and macro scales [12]. Starting with the macroscopic twist effect, which is achieved through the ingenious integration of chirality within a unit cell, the effect becomes apparent when an externally applied axial deformation is imposed on the structure [13, 14]. An additional intriguing implication of the chiral effect is the auxetic effect, which is characterized by a negative Poisson's ratio. This implies that the metastructure showcases a negative ratio between the lateral strain and axial strain [15, 16]. By incorporating chirality into the unit cell, the studied structure gains extra degrees of freedom beyond those inherent in the Cauchy elasticity [17, 18]. These supplementary degrees of freedom, (e.g. local rotation

and couple stress) can enable metastructures to exhibit acoustic activity similar to optical activity, where the polarization axis rotates during wave propagation [19, 20]. As waves propagate through such acoustically active mediums, a linearly polarized elastic wave undergoes polarization state rotation, leading to a circular polarization profile emerging during spreading [21]. This transition from linearly polarized to orthogonally polarized states is influenced by the chirality of the medium, leading to a transformation in the polarization state. In 1968, Portigal and Burstein showed this phenomenon where chirality is under consideration, proposing that a crystal exhibiting optical activity also manifests acoustic activity, resulting in a rotation of the polarization plane [22]. The rotation of polarization states introduces an extra wave characteristic that can be controlled, specifically the polarization state, similarly to the circular birefringence in optics. Moreover, it has been evidenced that chiral substances exhibit a selective affinity towards sound waves with a particular chirality, which is predicated upon the sound's ability to convey Orbital Angular Momentum (OAM) in the form of vortices [23, 24]. However, OAM can also be attained in centrosymmetric structures, such as in planar layer resonators and planar arrays of electroacoustic transducers [25, 26].

In this study, we demonstrate for the first time that a 3D chiral mechanical meta-structure is capable of transforming a longitudinally polarized wave into a transversely polarized wave. This conversion is attributed to the incorporation of additional degrees of freedom stemming from the chiral effect, specifically in the manifestation of rotational inertia. The latter mechanism is commonly identified in chiral mechanical metamaterials, rendering our metastructure comparable to its analogs with the distinctive characteristic of exhibiting energy transfer between modes. We use Finite Element Analysis (FEA) to assess the dispersion diagrams, the total displacement distribution, and the polarization state of the transmitted and reflected waves upon encountering both a periodic arrangement and single homogeneous block, achiral, and chiral unit cells. Additionally, we utilize a classical mass-spring model to theoretically describe the dispersion mode associated with the conversion effect that arises from the coupling of longitudinal and rotational behavior within the chiral unit cell.

2. Geometry definition and dispersion diagrams

Initially, we describe the features of the two main 3D mechanical metastructure designs under investigation. The schematic designs of the non-centrosymmetric and centrosymmetric structures are depicted in figures 1(a) and (b), respectively. Both have a lattice constant a and wings angled at $\alpha = 45°$. All other parameters are depicted in the figure caption.

In the achiral case illustrated in figure 1(d), the top-down and left-right connections are precisely orthogonal to the long arms of the connections, with a lateral length of h_1, and a width of w_1. Meanwhile, in the chiral configuration, all connections undergo a rotation of $\theta = 70°$, with the long and short arms denoted as d_2 and d_1, respectively, form an angle of $\varphi = 70°$, as depicted in figure 1(c). This inclination angle θ, defined as the angle between the triangular bases and the inclined connectors, is specifically set at 70°. This angle serves the dual purpose of introducing chirality within the unit cell, coupled with the manifestation of a rotational inertia-amplifying mechanism. It is noteworthy that the use of this angle value is intended to confirm the proof of concept for our structural conversion capability. Furthermore, the preference for triangular bases within the unit cell over simple square bases stems from the fact that the triangular case promotes more energy exchange between modes. All other geometrical parameters can be found in figure 1. Here, we consider the elastic wave propagating along the [001] crystallographic direction with wavenumber k_z, where $\vec{k} = (0, 0, k_z)$. The material has a density of $\rho = 1140\ \mathrm{kg\,m^{-3}}$, a Poisson ratio of $\nu = 0.4$ and a Young modulus of $E = 4.2$ GPa. Figures 2(a) and (b) delineate the band structure of achiral and chiral metamaterials, respectively, showing all viable modes that may propagate along the ΓZ direction. It is worth noting that, the total displacement portrayed in figures 2(c) and (d) depicts the normal longitudinal and rotation coupled-longitudinal motions exhibited by the achiral and chiral metastructures, respectively. The red arrows in the field maps denote the direction of displacement at points A and B, corresponding to a specific value of $k_z = \pi/2a$.

3. Mathematical mass-spring formulation

To explore the fundamental process for polarization conversion, we employ the standard two-dimensional chiral mass-in-mass unit cell, characterized by a classical monoatomic lattice system [27, 28]. This basic discrete model has been extensively used for various analytical endeavors, especially in investigating the dispersion relation of elastic waves [29–32]. Figure 3 shows the mass-spring model used that includes a central mass denoted by M, which is connected through linear springs that are inclined and exhibit a stiffness constant designated as D_1^{kl}, where $k, l \in \{z, y, \varphi\}$. This introduced an additional bending moment.

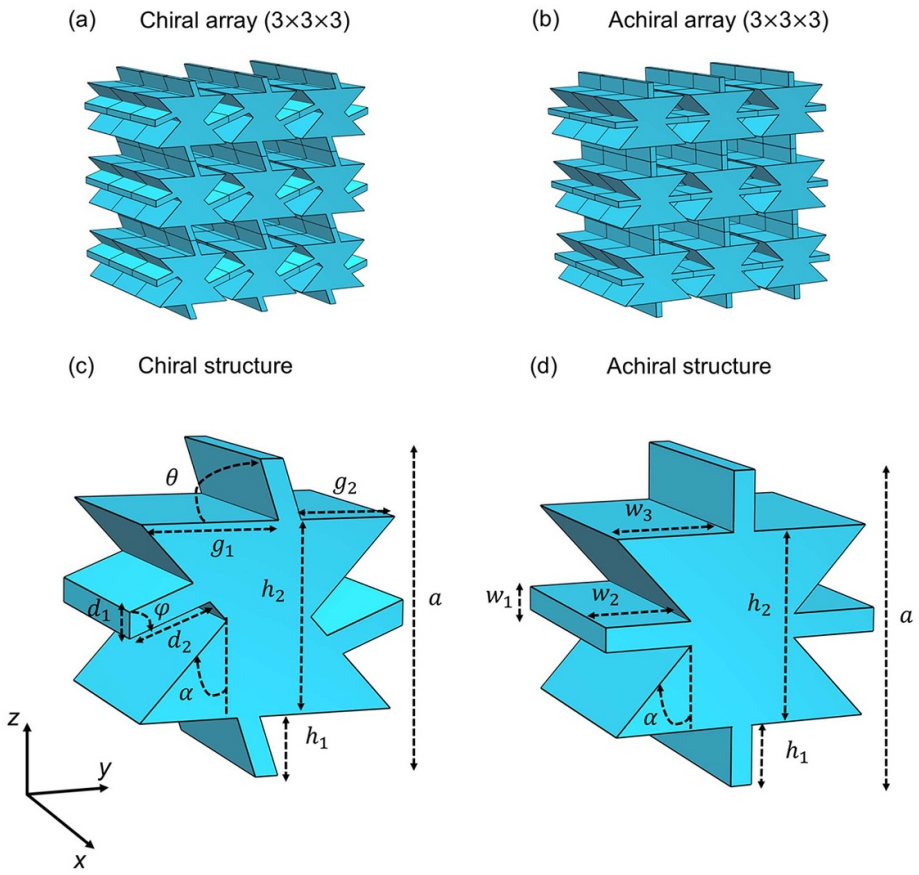

Figure 1. Geometrical description of the 3D arrays encompassing chiral (a) and achiral (b) metamaterial composed of $3 \times 3 \times 3$ unit cells, respectively. (c) and (d) The 3D schematic design of chiral and achiral unit cells with a uniform spatial period of a in all directions, respectively. The set of geometrical parameters are defined as follows: $a = 1.3$ cm, $h_1 = 0.25$ cm, $h_2 = 0.8$ cm, $d_1 = 0.1$ cm, $d_2 = 0.4$ cm, $w_1 = 0.1$ cm, $w_2 = 0.4$ cm, $w_3 = 0.55$ cm, $g_1 = 0.63$ cm, $g_2 = 0.45$ cm, $\alpha = 45°$, $\varphi = 70°$ and $\theta = 70°$.

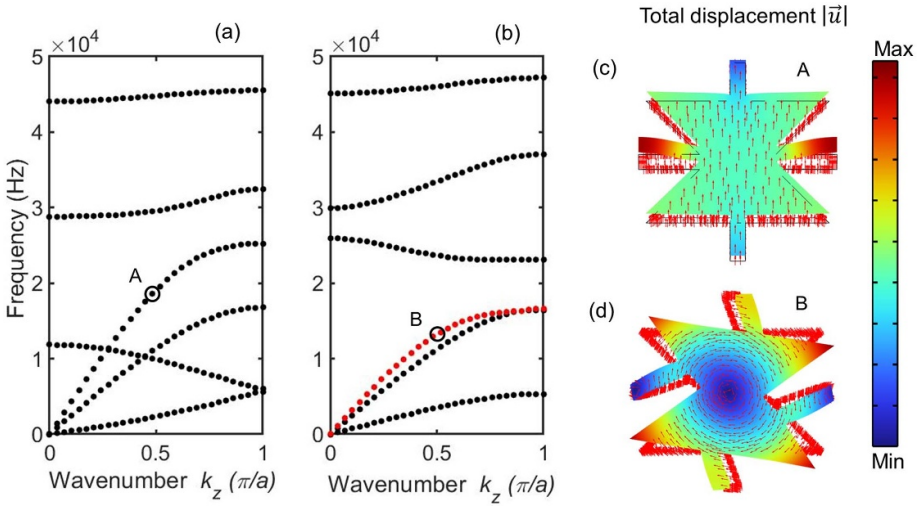

Figure 2. The dispersion diagrams for the achiral and the chiral metamaterials are presented in (a) and (b), respectively. The red dotted curve in (b), depicts the rotational coupled compressional mode. Both metamaterials have the same spatial period of $a_x = a_y = a_z = a$ along all directions, with a wavenumber k_z within the range of $[0, \pi/a]$. In (c) and (d), the entire field distribution (normalized displacement in the false color and an exaggerated deformation for better clarification) is illustrated when the wavenumber $k_z = \pi/2a$ for the achiral and chiral metamaterials, respectively. The red arrows in (c) and (d) present the direction of the displacement field distributions at points A and B, respectively.

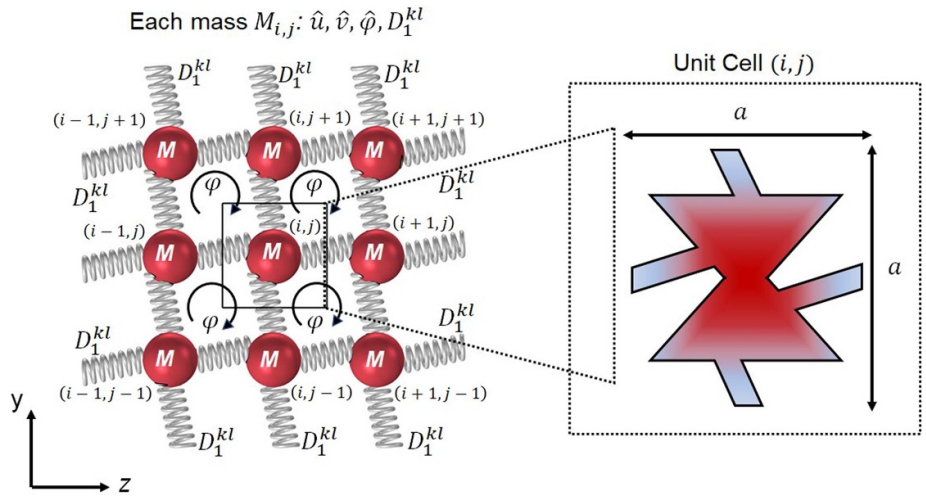

Figure 3. The monoatomic mass-spring model consists of a mass-in-mass unit cell, where the central mass M is represented by a red dot. The masses are interconnected to their nearest neighbors via inclined springs featuring a stiffness coefficient of D_1^{kl}. The indices (i), (j) correspond to the row and column coordinates of the masses M within the system. The fundamental unit cell exhibits a periodicity of $a = 1.3$ cm. The incorporation of the aforementioned inclined connections within this configuration engenders heightened bending inertia, thereby leading to an amplified micro-rotational motion.

Newton's second law of dynamics expounded the total forces acting on the (i, j) mass M, which can be expressed as follows [33]:

$$M\frac{\partial^2 u_{i,j}^z}{\partial t^2} = D_1^{zz}(u_{i,j+1}^z + u_{i,j-1}^z - 2u_{i,j}^z) + D_1^{zy}(v_{i+1,j}^y - v_{i-1,j}^y) + D_1^{z\varphi}(\varphi_{i,j+1} - \varphi_{i,j-1}) \tag{1}$$

$$M\frac{\partial^2 v_{i,j}^y}{\partial t^2} = D_1^{yy}(v_{i+1,j}^y + v_{i-1,j}^y - 2v_{i,j}^y) + D_1^{yz}(u_{i,j+1}^z - u_{i,j-1}^z) + D_1^{y\varphi}(\varphi_{i+1,j} - \varphi_{i-1,j}) \tag{2}$$

By incorporating chirality through the inclined connection in the unit cell, a bending moment is generated, which can be explicitly delineated in the following manner (using the rotation inertia J) [34, 35]:

$$J\frac{\partial^2 \varphi_{i,j}}{\partial t^2} = D_1^{\varphi z}(u_{i,j+1}^z - u_{i,j-1}^z) + D_1^{\varphi y}(v_{i+1,j}^y - v_{i-1,j}^y) + D_1^{\varphi\varphi}(\varphi_{i,j+1} + \varphi_{i,j-1} - 2\varphi_{i,j}) \tag{3}$$

By considering harmonic solutions to equations (1)–(3), the periodic conditions can be formulated as follows [36, 37]: $u_{i,j\pm m}^z = e^{i(\pm mka-\omega t)}u_n$, $v_{i\pm m,j}^y = e^{i(\pm mka-\omega t)}v_n$, and $\varphi_{i,j\pm m} = \varphi_{i\pm m,j} = e^{i(\pm mka-\omega t)}\varphi_n$, where k and a are the wavenumber throughout the ΓZ direction and the unit cell period, respectively. The substitution of the Bloch solutions into the governing, equations (1)–(3), leads to the following matrix:

$$\begin{bmatrix} 2D_1^{zz}(cos(ka)-1)+M\omega^2 & 2iD_1^{zy}sin(ka) & 2iD_1^{z\varphi}sin(ka) \\ 2iD_1^{yz}sin(ka) & 2D_1^{yy}(cos(ka)-1)+M\omega^2 & 2iD_1^{y\varphi}sin(ka) \\ -2iD_1^{\varphi z}sin(ka) & -2iD_1^{\varphi y}sin(ka) & 2D_1^{\varphi\varphi}(cos(ka)-1)+J\omega^2 \end{bmatrix} \begin{bmatrix} u_n \\ v_n \\ \varphi_n \end{bmatrix} = 0 \tag{4}$$

In order to obtain the solutions for this system of equations indicated in equation (4), we need to solve the roots of a polynomial equation with a degree of six, as outlined in equation (5).

$$A\omega^6 + B\omega^4 + C\omega^2 + D = 0 \tag{5}$$

The expressions of the coefficients denoted as A, B, C, and D in equation (5) are given as:

$$\begin{cases} A = JM^2 \\ B = 2[cos(ka)-1](JM(D_1^{zz}+D_1^{yy}) + M^2D_1^{\varphi\varphi}) \\ C = 4[cos(ka)-1]^2(JD_1^{zz}D_1^{yy} + MD_1^{zz}D_1^{\varphi\varphi} + MD_1^{yy}D_1^{\varphi\varphi}) - 4sin^2(ka)[JD_1^{zy}D_1^{yz} + MD_1^{z\varphi}D_1^{\varphi z}] \\ D = 8D_1^{zz}D_1^{yy}D_1^{\varphi\varphi}[cos(ka)-1]^3 + 8[cos(ka)-1]sin^2(ka)[D_1^{zy}D_1^{yz}D_1^{\varphi\varphi} - D_1^{z\varphi}D_1^{\varphi z}D_1^{yy}] \\ \quad + i8sin^3(ka)[D_1^{zy}D_1^{\varphi z}D_1^{\varphi y} + D_1^{z\varphi}D_1^{yz}D_1^{\varphi y}] \end{cases} \tag{6}$$

By implementing a variable substitution of $\omega = \sqrt{\Omega - \frac{B}{3A}}$, the sixth-degree equation represented by equation (5) was transformed into the depressed cubic equation form, as indicated by equation (7).

$$\Omega^3 + \underbrace{\frac{(3AC - B^2)}{3A^2}}_{p}\Omega + \underbrace{\frac{(2B^3 - 9ABC + 27DA^2)}{27A^3}}_{q} = 0 \tag{7}$$

Furthermore, it is noteworthy that the solution to a depressed cubic formula is well known within diverse mathematical frameworks [38–40]:

$$\Omega_1 = r - \frac{B}{3A}, \quad \Omega_2 = r\left(-\frac{1}{2} + i\frac{\sqrt{3}}{2}\right) - \frac{B}{3A}, \quad \Omega_3 = r\left(-\frac{1}{2} - i\frac{\sqrt{3}}{2}\right) - \frac{B}{3A} \tag{8}$$

The coefficients upon which the solutions depend are formulated in the following manner:

$$r = e + f, \quad e = \left(-\frac{q}{2} + \sqrt{\frac{q^2}{4} + \frac{p^3}{27}}\right), \quad f = \left(-\frac{q}{2} - \sqrt{\frac{q^2}{4} + \frac{p^3}{27}}\right) \tag{9}$$

Consequently, the roots of the system of equation (4) are written as follows:

$$\omega_1 = \sqrt{\Omega_1}, \quad \omega_2 = \sqrt{\Omega_2}, \quad \omega_3 = \sqrt{\Omega_3}, \quad \omega_4 = -\sqrt{\Omega_1}, \quad \omega_5 = -\sqrt{\Omega_2}, \quad \omega_6 = -\sqrt{\Omega_3} \tag{10}$$

The plus and minus signs in the eigenfrequencies in equation (10) relate to the propagation of forward and backward waves. Henceforth, we focus on determining the corresponding eigenvectors for these eigenfrequencies in order to identify the parameters that govern the conversion of compressional modes to shear modes. To facilitate this analysis, we simplify the set of equations represented by equation (4) and make the simplifying assumption that the coefficients $C_{zy} = C_{yz}$ and $C_{z\varphi} = C_{y\varphi}$ are approximately equal.

$$\begin{bmatrix} C_{zz} + M\omega_i^2 & C_{zy} & C_{z\varphi} \\ C_{zy} & C_{yy} + M\omega_i^2 & C_{z\varphi} \\ -C_{z\varphi} & -C_{z\varphi} & C_{\varphi\varphi} + J\omega_i^2 \end{bmatrix} \begin{bmatrix} u_n \\ v_n \\ \varphi_n \end{bmatrix} = 0 \tag{11}$$

$$\begin{bmatrix} C_{zz} + M\omega_i^2 - C_{zy} & C_{zy} & C_{z\varphi} \\ 2C_{zy} - 2M\omega_i^2 - C_{zz} - C_{yy} & C_{yy} + M\omega_i^2 - C_{zy} & 0 \\ 0 & -C_{z\varphi} & C_{\varphi\varphi} + J\omega_i^2 \end{bmatrix} \begin{bmatrix} u_n \\ v_n \\ \varphi_n \end{bmatrix} = 0 \tag{12}$$

The manipulation of equation (11) results in three pondering coefficients that relate the compressional displacement $\hat{u}$, the shear displacement $\hat{v}$, and the in-plane rotation $\hat{\varphi}$, as indicated by equation (14).

$$(2C_{zy} - C_{zz} - C_{yy} - 2M\omega_i^2)\hat{u} + (C_{yy} - C_{zy} + M\omega_i^2)\hat{v} = 0 - C_{z\varphi}\hat{v} + (C_{\varphi\varphi} + J\omega_i^2)\hat{\varphi} = 0 \tag{13}$$

$$\hat{v} = \underbrace{\frac{(-2C_{zy} + C_{zz} + C_{yy} + 2M\omega_i^2)}{(C_{yy} - C_{zy} + M\omega_i^2)}}_{\beta(\omega_i^2)}\hat{u}, \quad \hat{\varphi} = \underbrace{\frac{C_{z\varphi}}{(C_{\varphi\varphi} + J\omega_i^2)}}_{\gamma(\omega_i^2)}\hat{v}, \quad \alpha(\omega_i^2) = -(C_{zy}\beta + C_{z\varphi}\gamma) \tag{14}$$

Subsequently, the set of eigenvectors $\Psi_{\omega_i^2}$ can be expressed in terms of the pondering coefficients $\alpha(\omega_i^2)$, $\beta(\omega_i^2)$ and $\gamma(\omega_i^2)$.

$$\Psi_{\omega_i^2} = \begin{bmatrix} \alpha(\omega_i^2) \\ \beta(\omega_i^2) \\ \gamma(\omega_i^2) \end{bmatrix} \hat{u}, \text{with } \hat{u} = \frac{\vec{u}}{\|\vec{u}\|} \tag{15}$$

Most importantly, the resultant eigenvectors are linearly dependent on the longitudinal component $\hat{u}$, as opposed to usual circumstances where the eigenvectors are totally independent, i.e. the coefficients $\beta(\omega_i^2)$ and $\gamma(\omega_i^2)$ were equal to zero. The eigenvectors $\Psi_{\omega_i^2}$ are used to derive the polarization states of the eigenfrequencies ω_i using equation (16) in its general 3D format [41].

$$P_\zeta = \frac{\iiint_{V_i} \sqrt{|\Psi_{\omega_\zeta^2}|^2}\, dr}{\iiint_{V_i} \sqrt{|\Psi_{\omega_\alpha^2}|^2 + |\Psi_{\omega_\beta^2}|^2 + |\Psi_{\omega_\gamma^2}|^2}\, dr}, \zeta \in \{\alpha, \beta, \gamma\} \tag{16}$$

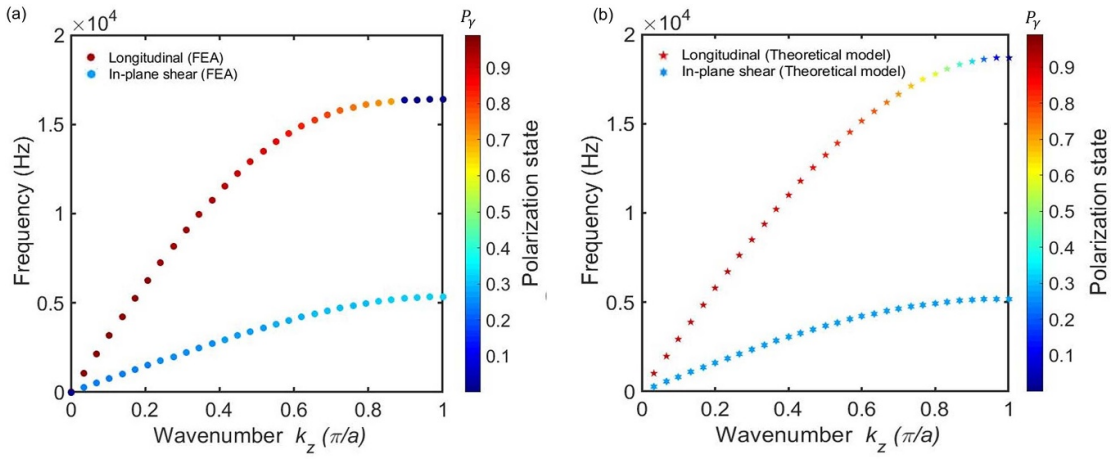

Figure 4. (a), (b) The diagrams illustrate the energy-momentum characteristics of compressional and shear motions in the chiral metastructure obtained using the FEA method and the theoretical model, respectively. The dotted point plot corresponds to the results of the FEA simulation conducted on the chiral metamaterial, for both compressional and in-plane shear modes. The stars correspond to the longitudinal and in-plane shear acoustic branches, as obtained through employment of the monoatomic spring mass model with inclined connection. The scale bar pertains to the longitudinal polarization state along the ΓZ direction, for both cases.

It is important to notice that the subscript notation ζ represents three distinct characters: α, β, and γ. The latter characters correspond, respectively, to the displacement components along the Cartesian coordinates y, x, and z. As the out-of-plane mode is decoupled from the in-plane and longitudinal modes, we restrict the mathematical investigation to the two-dimensional case, where only longitudinal and shear horizontal waves can exist. The parameters V_i typically present the volume of the unit cell, but in 2D, they are reduced to the unit cell's in-plane surface. The present analysis intends to compare the conversion results obtained through the FEA. However, this approach is incompatible with eigenmode computation and is confined to evaluating energy exchange via the linear dependence of the eigenvectors. By employing the information derived from equations (10) and (16), figures 4(a) and (b) show a notable consistency between the analytical model and the numerical results, except for the longitudinal case when the wavelength is in the order of magnitude of the structural periodicity. The latter divergence results from the coupling of longitudinal mode and optical branches, which is not taken into consideration in the mathematical model. Furthermore, using this theoretical combination to delineate the eigenfrequencies (mode shapes) and eigenvectors (polarization states), three main domains can be discerned. In the low wavenumber domain ($k_z < 0.4\pi/a$), the polarization of the modes shows negligible alterations. In figures 4(a) and (b), only longitudinal polarization is evident, indicated by the red star and dotted curves, while the absence of in-plane shear polarization is denoted by the blue colour in this range. In the mid-range domain ($0.4\pi/a < k_z < 0.8\pi/a$), the onset of polarization conversion is denoted by the alteration in colour of the dotted and star curves from red to yellow for longitudinal polarization and from blue to cyan for the in-plane shear modes (see figures 4(a) and (b). Additionally, in the large wavenumber domain ($0.8\pi/a < k_z < \pi/a$), the longitudinal dotted and star curves assume a blue, indicating a shift from longitudinal to shear modes, as shown in figures 4(a) and (b). In our analysis, we confined the theoretical model to the initial two acoustic branches, focusing on the longitudinal and in-plane shear waves, as they represent the predominant modes exhibiting energy exchange. It is worth noting that the coupling coefficients D_1^{zy} and $D_1^{z\varphi}$ have two distinct values. The first represents the strong coupling regime, characterized by a high degree of energy interplay between rotation and compression. In contrast, the second reflects the weak coupling regime, characterized by limited energy communication to the in-plane shear mode (shear horizontal), since the compressional mode exhibits stronger coupling than the in-plane shear mode. Subsequently, we present the set of the mass-spring parameters employed for the evaluation of the longitudinally-coupled mode with rotation: $M = 4 \times 10^{-3}$ kg, $J = 0.8 \times 10^{-4}$ kg m^2, $a = 1.3 \times 10^{-2}$ m, $D_1^{zz} = 3.5 \times 10^3$ N m^{-1}, $D_1^{yy} = 7 \times 10^3$ N m^{-1}, $D_1^{zy} = 4 \times 10^2$ N m^{-1}, $D_1^{z\varphi} = 3.2 \times 10^3$ N m^{-1}, $D_1^{\varphi\varphi} = 7 \times 10^3$ N m^{-1}. In the context of the in-plane shear mode, only the coupling coefficients $D_1^{zy} = 1.5 \times 10^{-1}$ N m^{-1} and $D_1^{z\varphi} = 1 \times 10^{-1}$ N m^{-1} are modified and tuned.

4. Results and discussion

In this section, we consider numerical modeling using FEA to evaluate the chiral meta-structure's ability to convert longitudinal waves into both horizontal and vertical shear waves. Our approach employs an eigenvalue problem to scrutinize the polarization states of each mode within the dispersion diagram for the chiral structure, as illustrated in figures 5(d)–(f). It is crucial to emphasize that we calculate the polarization states of the chiral metastructure modes using FEA according to equation (16), where V_i represents the unit cell volume this time. These illustrations provide evidence that the longitudinal mode is capable to transform P_γ to P_α and P_β polarization states, which results from the interaction of the longitudinal wave with rotational inertia. The total displacement field associated with the longitudinal mode distinctly displays the ability to merge compressional motion with an additional degree of freedom, namely rotational motion, as evidenced in figure 5(c). Moreover, harmonic analysis is conducted to evaluate the responses of a periodic arrangement featuring $1 \times 1 \times 6$ dimensions. Periodic conditions are applied on the x- and y-axes for homogeneous block, achiral, and chiral unit cells, respectively, to an external longitudinal vibration propagating along the z-axis, as illustrated in figure 6(a). A parallel assessment is conducted for a singular $1 \times 1 \times 1$ homogeneous block, achiral, and chiral unit cells without periodic conditions, as depicted in figure 6(b). These unit cells are enclosed by two large building blocks on both sides, composed of the same material as the unit cell, while two perfectly matched layers (PML) are implemented at the left and right boundaries to prevent any spurious reflection. Additionally, we use equation (16) to assess the polarization states of transmitted and reflected waves when they interact with a homogeneous block, achiral, and chiral metamaterials. Notably, in this case, we consider the volume integration denoted by V_i as the spatial volumes encompassing the right and left sectors of the array or unit cell, respectively. Where the index $i \in \{1,2\}$, as indicated in figures 6(a) and (b). By generating a wave on our structure from the left side, as depicted in figure 6(a), with a normalized longitudinal vibration and a maximum frequency of 1.8×10^4 Hz, propagating along the z-axis, we obtain the polarization states of the transmitted waves at the monitor located on the right side. This investigation encompasses homogeneous blocks, achiral, and chiral metamaterials, as exemplified in figures 7(a)–(c), respectively. The homogeneous block and the achiral arrays preserve the identical polarization state as the incident wave P_γ, as indicated by the cyan and blue colors, respectively. In other words, the value of P_γ remains constant at approximately one, signifying the absence of conversion. Conversely, the chiral meta-array can convert a purely longitudinal polarized wave to both horizontal P_α and vertical shear P_β waves, as represented by the red color. Similarly, the polarization states of reflected waves from the homogeneous block, achiral, and chiral meta-arrays are illustrated in figures 8(a)–(c), respectively. Furthermore, we evidence that the reflected waves undergo a transformation from a purely longitudinal polarization, P_γ, to alternative polarization states, P_α and P_β, upon their interaction with the interface of the chiral meta-array. Conversely, in the case of the homogeneous block and achiral arrays, the polarization states of the reflected waves remain unaltered. The 3D distribution of the total field displacement for the homogeneous, achiral, and chiral arrays is presented in figures 9(a)–(c). At the identical frequency of 5.5 kHz, the field maps distinctly illustrate that the polarization state of both transmitted and reflected waves remains consistent with the external longitudinal stimulus for both homogeneous and achiral arrays, as depicted in figures 9(a) and (b). Conversely, in the scenario involving the chiral array, the polarization of both transmitted and reflected waves at the same frequency switches from longitudinal to orthogonal polarization (shear), as shown in figure 9(c). This outcome confirms the chiral meta-array's capability to effectuate a 90° rotation in the polarization state.

Henceforth, we confine our investigation to the case of a single unit cell, considering the geometric design illustrated in figure 6(b). It is noteworthy that all parameters and physical properties remain the same as before, with the array being replaced by a single unit cell this time. Figures 10(a)–(c) and 11(a)–(c) illustrate that a single chiral meta-atom can induce an elastic polarization conversion similar to its bulk counterpart, represented by the periodic arrangement of unit cells. This relies on the presence of shear components in both the transmitted and reflected waves ($P_\alpha \neq 0$ and $P_\beta \neq 0$), as denoted by the red curves. However, in scenarios involving homogeneous and achiral unit cells, the polarization state remains invariant ($P_\alpha = 0$ and $P_\beta = 0$), aligning with the incident vibration (longitudinal). In the homogeneous case, the polarization state of both transmitted and reflected waves remains unaltered from the incident wave, denoted as P_γ, as depicted in figure 12(a) around 12 kHz. The achiral structure's total displacement field also preserves the same polarization state as the incident excitation throughout the entire spectral range, as exemplified at the frequency of 2.404 kHz in figure 12(b). In contrast, in figures 12(c) and (d), the chiral case manifests the ability to convert both transmitted and reflected waves from longitudinal polarization to shear polarization at the frequencies of 2.404 kHz and 10.598 kHz, respectively.

Additionally, a time-harmonic vibration with a sinusoidal waveform was employed to explore the polarization states of transmitted waves through a homogeneous block, achiral and chiral metamaterials. The

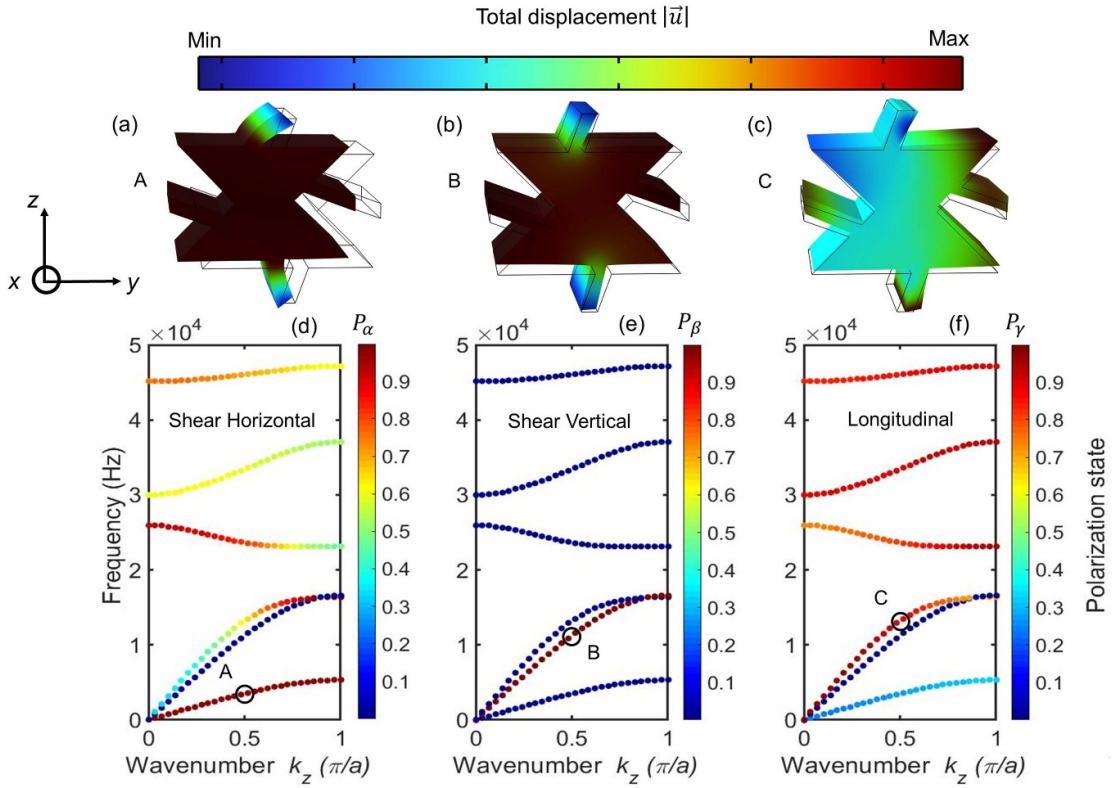

Figure 5. Panels (a)–(c) depict the total displacement behaviors of shear horizontal, shear vertical, and rotational-coupled longitudinal motion at the points A, B, and C indicated by the circle in each respective polarization. Panels (d)–(f) portray the polarization state of the primary triad of modes; namely, shear horizontal P_α, shear vertical P_β, and longitudinal P_γ polarizations, respectively.

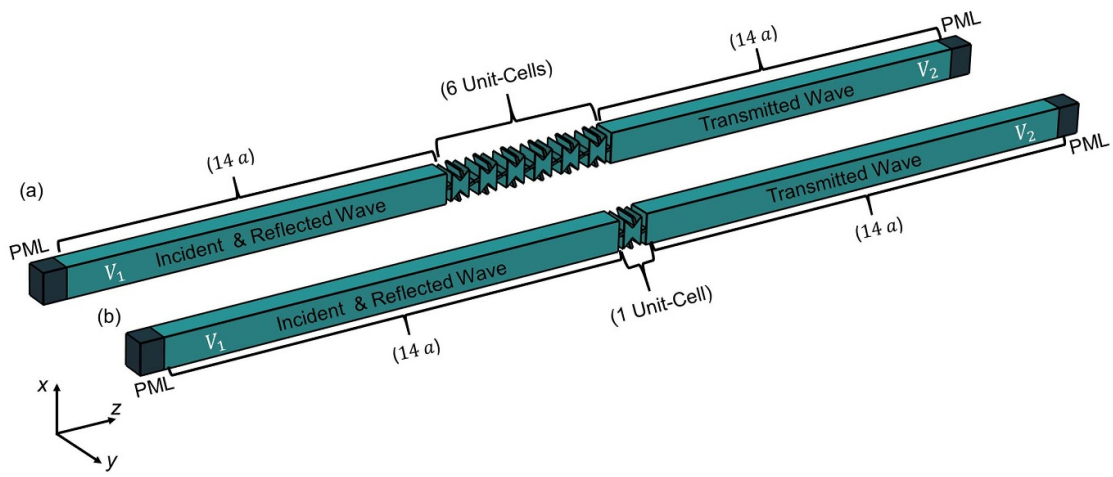

Figure 6. (a), (b) The three-dimensional schematic representation used for evaluating the polarization state of both transmitted and reflected waves upon interacting with an array of unit cells and a single unit cell, respectively.

vibration, directed along the z-axis, possesses a normalized magnitude and a frequency of 2.404 kHz, with its duration varying from 0 to 5 ms, as indicated by the black curve in figure 13(a). The findings indicated that the polarization states of transmitted waves remained unchanged when the homogeneous block and achiral unit cells were stimulated by the incident vibration. This outcome is demonstrated by the pink curves in figures 13(b) and (c), where the output showed only the P_γ component, while the P_α and P_β components remained at zero, as depicted by the red and dark-blue curves, respectively. In contrast, the chiral structure caused the incident compressional vibration to be transformed into a shear vibration, as indicated by the results presented in figure 13(d). As a result, the output signal clearly displays the presence of the P_α component, which corresponds to the shear component. Finally, figures 14(a)–(c) display the overall

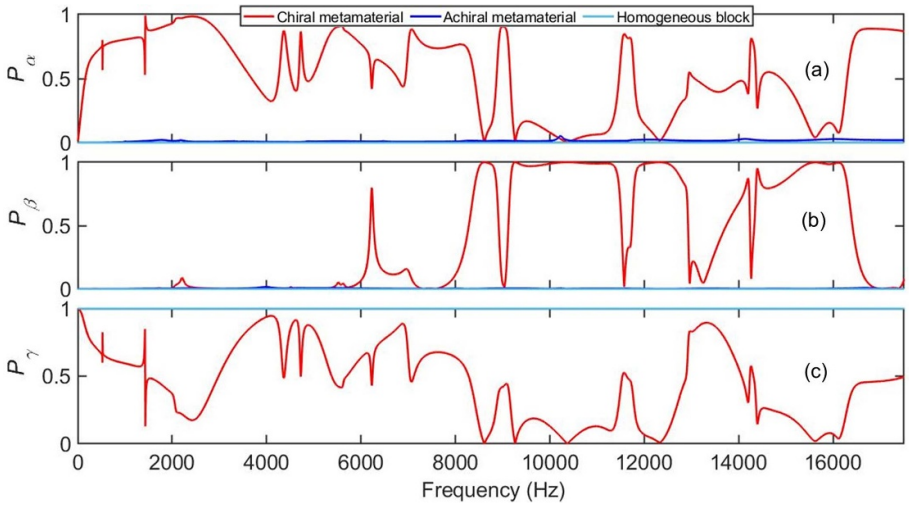

Figure 7. (a)–(c) Polarization states of transmitted waves subsequent to encountering a periodic arrangement of $1 \times 1 \times 6$ unit cells for homogeneous blocks, achiral configurations, and chiral structure, respectively.

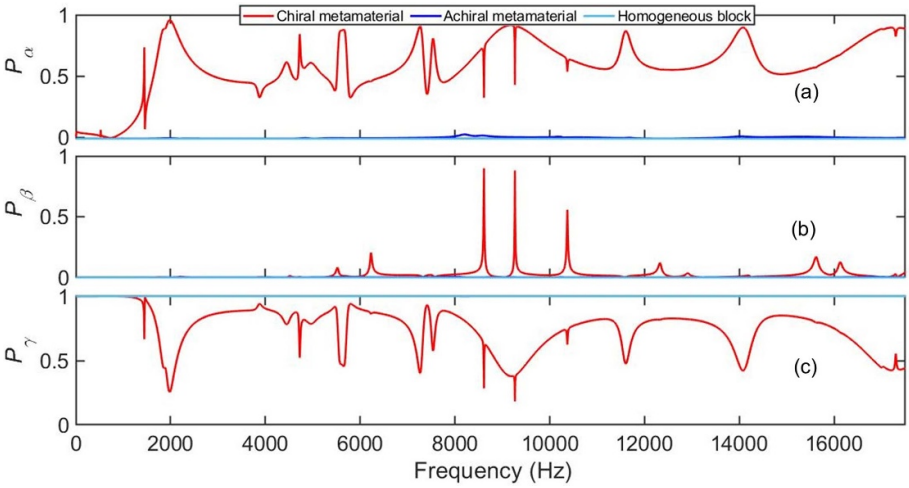

Figure 8. The illustrations labeled (a), (b), and (c) portray the polarization state of the elastic wave upon reflection at the interface of a meta-array composed of $1 \times 1 \times 6$ unit cells for a homogeneous cube, an achiral meta-atom, and a chiral meta-atom, respectively.

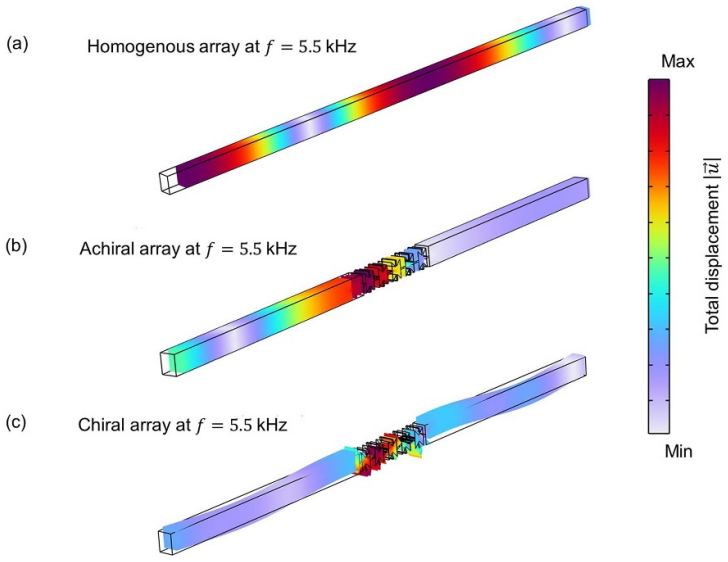

Figure 9. Panels (a)–(c) present the total displacement field of a homogeneous block, achiral, and chiral arrays at a frequency of 5.5 kHz, respectively.

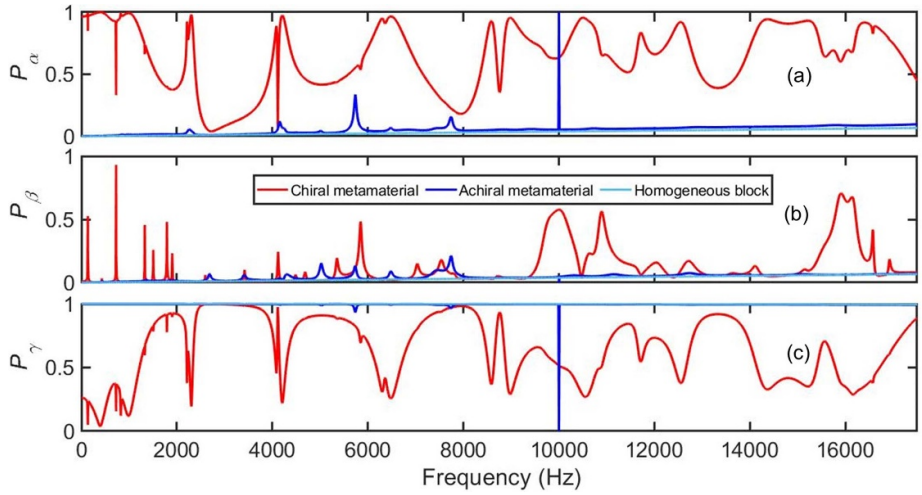

Figure 10. The diagrams (a), (b), and (c) depict the polarization state of the transmitted elastic wave following interaction with a single unit cell of a homogeneous block, an achiral, and a chiral configurations, respectively.

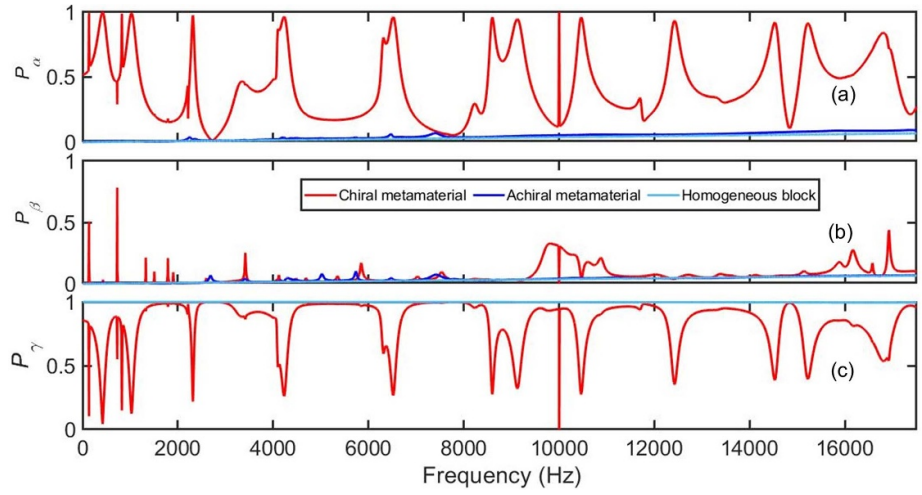

Figure 11. Diagrams (a), (b), and (c) elucidate the polarization state of the elastic wave upon reflection at the interface of a single unit cell of a homogeneous block, an achiral meta-atom, and a chiral meta-atom, respectively.

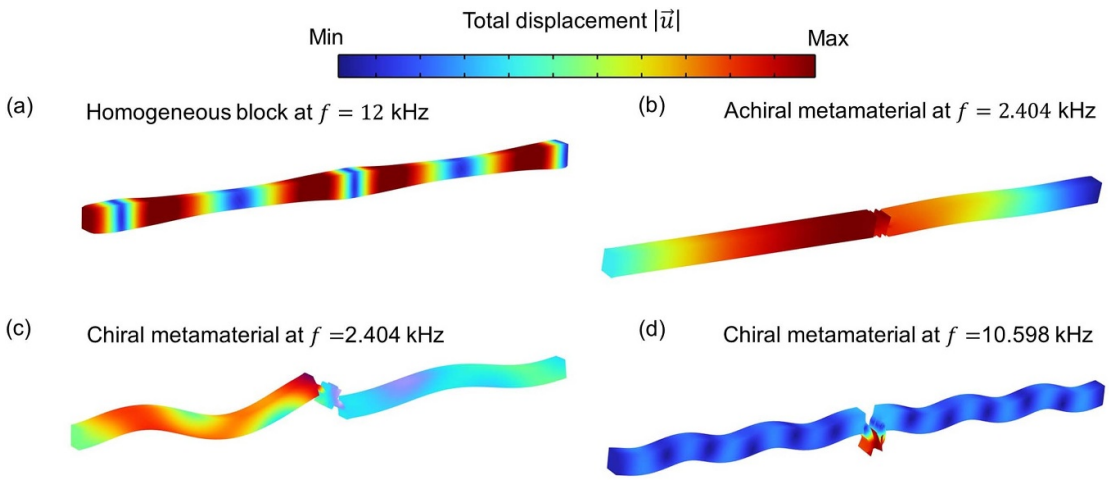

Figure 12. Panels (a) and (b) present the total displacement field of a homogeneous block and an achiral unit cell, respectively, at the frequencies of 12 kHz and 2.404 kHz. In contrast, panels (c) and (d) display the total displacement field of the chiral metamaterial unit cell at the frequencies of 2.404 kHz and 10.598 kHz, respectively.

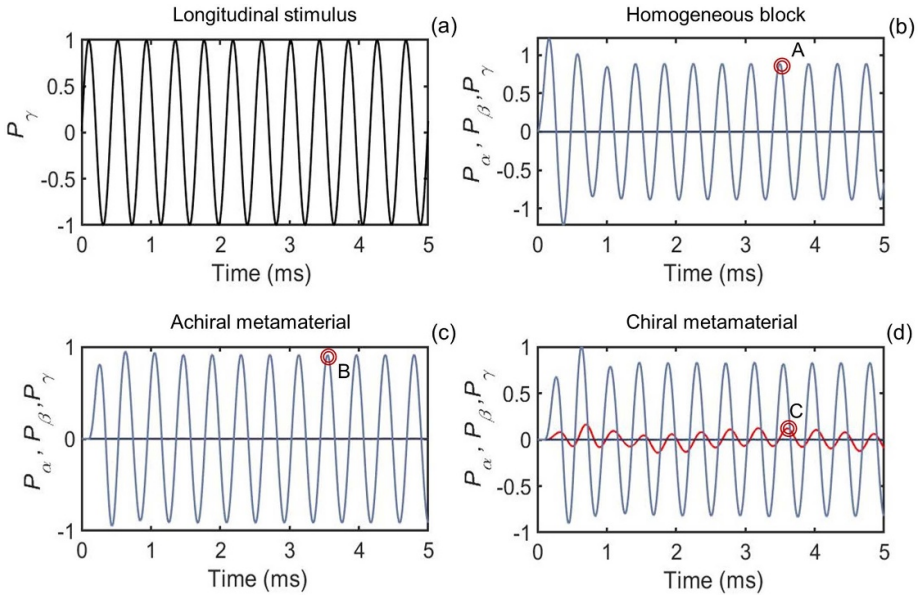

Figure 13. In panel (a), a longitudinal sinusoidal excitation source with a normalized magnitude of 1 and a frequency of 2.404 kHz, directed along the z-direction, as indicated by the black curve. Panels (b)–(d) portray the polarization states of a time-harmonic stimulus after encountering a homogeneous block, as well as achiral and chiral metastructures, respectively. The fundamental polarizations of the transmitted wave, specifically shear horizontal P_α, shear vertical P_β, and longitudinal P_γ for all cases, are delineated in red, dark-blue, and pink, respectively.

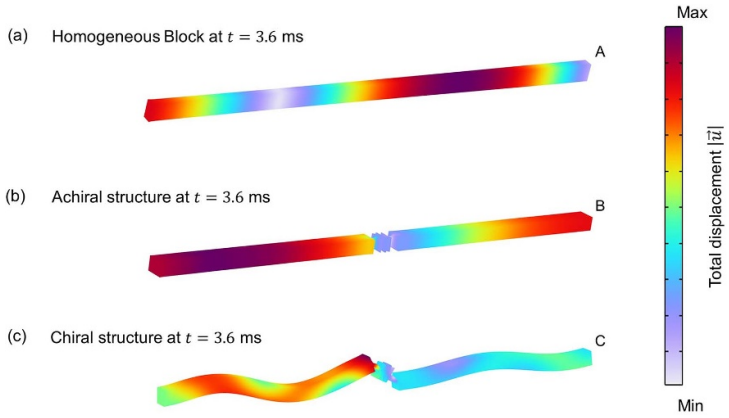

Figure 14. Panels (a)–(c) depict the total displacement field at a time step of $t = 3.6$ ms, as denoted by the points A, B and C in figure 13, for the homogeneous, achiral, and chiral meta-atoms, respectively.

displacement field at a specific time of 3.6 ms for all cases, revealing a remarkable degree of consistency between the frequency and time-harmonic investigations carried out in this study.

5. Conclusion

Within the scope of this study, we present a compelling analysis of 3D structure facilitating polarization state conversion in solid materials. Our investigation focuses on the mechanical properties of achiral and chiral metastructures. Initially, a rotational inertia-amplifying mechanism is introduced into the chiral metastructure through its inherent chirality, thereby inducing a rotation in the polarization plane. The absence of rotational inertia prevents achiral structures and homogeneous media from yielding comparable outcomes. Subsequently, we have demonstrated that the incorporation of chiral effects endows the normal meta-atom with an additional degree of freedom, which enables rotational motion and conversion of the polarization state in both time and frequency domain simulations. These findings demonstrate that

including chirality enables the structure's conversion ability by establishing a hybrid mode via compressional and rotational movements. Notably, this conversion leads to the transformation of longitudinal waves into corresponding orthogonal polarizations, i.e. shear waves. Additionally, the examined chiral structure manifests its capacity to transform the polarizations of both transmitted and reflected waves. Moreover, this conversion capacity is confirmed in both periodic chiral array and individual chiral metastructure scenarios. It is essential to emphasize that the inverse process of converting incoming shear waves into longitudinal ones is also feasible, and vice versa. A comparable polarization conversion can be attained in beam-based metastructures, given our belief that the latter maintain analogous features to their meta-atoms.

Data availability statement

The data cannot be made publicly available upon publication because no suitable repository exists for hosting data in this field of study. The data that support the findings of this study are available upon reasonable request from the authors.

Acknowledgments

This work is supported under the UTT Project Stratégique NanoSPR (OPE-2022-0293) and the Graduate School (Ecole Universitaire de Recherche) 'NANOPHOT' (ANR-18-EURE-0013). Financial support of Nano'Mat (www.nanomat.eu) by the Ministére de l'enseignement supérieur et de la recherche, the Conseil régional grand est, the FEDER fund and the Conseil général de l'Aube are also acknowledged. S G is also funded by UK Research and Innovation (UKRI) under the UK government's Horizon Europe funding uarantee, Grant Number 10033143.

ORCID iDs

Muamer Kadic https://orcid.org/0000-0002-4692-5696
Shuwen Zeng https://orcid.org/0000-0003-2188-7213

References

[1] Wong Z J, Wang Y, O'Brien K, Rho J, Yin X, Zhang S, Fang N, Yen T J and Zhang X 2017 *J. Opt.* **19** 084007
[2] Fedotov V A, Mladyonov P L, Prosvirnin S L, Rogacheva A V, Chen Y and Zheludev N I 2006 *Phys. Rev. Lett.* **97** 167401
[3] Hentschel M, Schäferling M, Duan X, Giessen H and Liu N 2017 *Sci. Adv.* **3** e1602735
[4] Wu W, Hu W, Qian G, Liao H, Xu X and Berto F 2019 *Mater. Des.* **180** 107950
[5] Nieves M, Carta G, Jones I, Movchan A and Movchan N 2018 *J. Mech. Phys. Solids* **121** 387–408
[6] Fan Z and Govorov A O 2010 *Nano Lett.* **10** 2580–7
[7] Schreiber R, Luong N, Fan Z, Kuzyk A, Nickels P C, Zhang T, Smith D M, Yurke B, Kuang W and Govorov A O 2013 *Nat. Commun.* **4** 2948
[8] Pagès S, Lagugné-Labarthet F, Buffeteau T and Sourisseau C 2002 *Appl. Phys.* B **75** 541–8
[9] Wu J, Xu X, Su X, Zhao S, Wu C, Sun Y, Li Y, Wu F, Guo Z and Jiang H *et al* 2021 *Phys. Rev. Appl.* **16** 064018
[10] Mur-Petit J and Molina R A 2014 *Phys. Rev.* B **90** 035434
[11] Cui Y, Kang L, Lan S, Rodrigues S and Cai W 2014 *Nano Lett.* **14** 1021–5
[12] Qi C, Jiang F and Yang S 2021 *Composites* B **227** 109393
[13] Frenzel T, Kadic M and Wegener M 2017 *Science* **358** 1072–4
[14] Fernandez-Corbaton I, Rockstuhl C, Ziemke P, Gumbsch P, Albiez A, Schwaiger R, Frenzel T, Kadic M and Wegener M 2019 *Adv. Mater.* **31** 1807742
[15] Dudek K K, Martínez J A I, Ulliac G and Kadic M 2022 *Adv. Mater.* **34** 2110115
[16] Lakes R 1987 *Science* **235** 1038–40
[17] Eringen A C and Eringen A C 1999 *Theory of Micropolar Elasticity*
[18] Lakes R S and Benedict R L 1982 *Int. J. Eng. Sci.* **20** 1161–7
[19] Nowacki W 1986 *Theory of Asymmetric Elasticity* (Pergamon)
[20] Carta G, Jones I, Movchan N and Movchan A 2019 *Proc. R. Soc.* A **475** 20190313
[21] Frenzel T, Köpfler J, Jung E, Kadic M and Wegener M 2019 *Nat. Commun.* **10** 3384
[22] Portigal D and Burstein E 1968 *Phys. Rev.* **170** 673
[23] Tong Q, Li J and Wang S 2023 arXiv:2301.02526
[24] Tong Q and Wang S 2022 *Phys. Rev.* B **105** 024111
[25] Jiang X, Li Y, Liang B, Cheng J C and Zhang L 2016 *Phys. Rev. Lett.* **117** 034301
[26] Esfahlani H, Lissek H and Mosig J R 2017 *Phys. Rev.* B **95** 024312
[27] Huang G and Sun C 2010 *J. Vib. Acoust.* **132** 031003
[28] Huang H, Sun C and Huang G 2009 *Int. J. Eng. Sci.* **47** 610–7
[29] Mead D 1973 *J. Sound Vib.* **27** 235–60
[30] Hussein M I 2009 *Phys. Rev.* B **80** 212301
[31] Manktelow K, Leamy M J and Ruzzene M 2011 *Nonlinear Dyn.* **63** 193–203
[32] Mork N, Kuchibhatla S A, Leamy M J and Fronk M D 2023 *Am. J. Phys.* **91** 56–63
[33] Eringen A C 2012 *Microcontinuum Field Theories: I. Foundations and Solids* (Springer Science & Business Media)

[34] Zhang H, Chen Y, Liu X and Hu G 2020 *J. Mech. Phys. Solids* **135** 103796
[35] Lee S W and Oh J H 2018 *Sci. Rep.* **8** 14243
[36] Lee E H and Yang W H 1973 *SIAM J. Appl. Math.* **25** 492–9
[37] Michel J C, Moulinec H and Suquet P 1999 *Comput. Methods Appl. Mech. Eng.* **172** 109–43
[38] Mukundan T 2010 *Resonance* **15** 347–50
[39] Saburov M and MAKh A 2015 *Sains Malays.* **44** 765–9
[40] Okoli O, Laisin M, Nsiegbe N and Eze A 2020 *COOU J. Phys. Sci.* **3** 515–21
[41] Achaoui Y, Khelif A, Benchabane S and Laude V 2010 *J. Phys. D: Appl. Phys.* **43** 185401